



## Crystal plasticity analysis of constitutive behavior of 5754 aluminum sheet deformed along bi-linear strain paths

M.A. Iadicola<sup>a,\*</sup>, L. Hu<sup>b</sup>, A.D. Rollett<sup>b</sup>, T. Foecke<sup>a</sup>

<sup>a</sup> Metallurgy Division, National Institute of Standards and Technology, US Department of Commerce, Gaithersburg, MD 20899-8553, United States

<sup>b</sup> Department of Materials Science and Engineering, Carnegie Mellon University, Pittsburgh, PA 15213, United States

### ARTICLE INFO

#### Article history:

Available online 24 March 2012

#### Keywords:

Aluminum alloy  
Biaxial  
Constitutive laws  
Crystals  
Diffraction  
Experimental techniques  
Hardening  
Micro-mechanics  
Microstructural  
Plasticity  
Relaxation  
Stress strain  
Tension  
Uniaxial  
Variable loading

### ABSTRACT

Sheet specimens of aluminum alloy 5754 were deformed along a series of bi-linear, equal-biaxial and uniaxial, strain paths while simultaneously measuring stress–strain behavior. The Visco-Plastic Self-Consistent crystal plasticity model, which incorporates texture evolution, was used to simulate the flow stress and hardening behavior based in part on the measured crystallographic texture before deformation. The predicted crystallographic texture qualitatively captures the texture measured in the experiments. Including latent hardening of multiple slip planes allowed the model to explain the decrease in flow stress when changing from equal-biaxial to uniaxial deformation. However, the model captures neither the details of the drop in flow stress nor the magnitude of the plastic hardening after the change in deformation mode. This is likely due to room temperature recovery between the two segments of testing.

Published by Elsevier Ltd.

### 1. Introduction

Predictions of failure in metal forming simulations that make use of forming limit curves or other criteria in stress suffer from a number of fundamental limitations. Since strain is not an intrinsic state variable, there is no single value that can universally represent the point of failure, and thus the limits of usable plastic strain are strong functions of the strain path (Hosford and Duncan, 1999). Work has recently begun to shift from a strain-based to a stress-based modeling scheme, which removes path dependence since stress is an intrinsic state variable, and the point of failure of a component can be identified by a single equivalent-stress value (Stoughton and Zhu, 2004). Stress-based forming limits have been proposed as more applicable to some advanced alloys being considered for automotive applications (Stoughton and Zhu, 2004), such as dual-phase and transformation-induced plasticity (TRIP) steels, in which flow stresses are high enough that the failure mode changes from ductile failure to decohesion, which is better described by a fracture stress than a strain to failure (Choi et al., 2009).

Transitioning from multi-axial strain space to multi-axial stress space requires a robust multi-axial constitutive relation that can accurately describe the evolution of the yield surface along any strain path. This requires information about how the yield surface evolves in stress space, which is difficult to measure, but is starting to be reported in the literature (Iadicola et al., 2008; Kuwabara, 2007; Yoshida et al., 2007; Andar et al., 2010). However, to develop an understanding that can predict the mechanical response of a given sheet metal, the yield-surface data must be tied to the structural characteristics of the material. A structural characteristic that shows promise is the initial and evolving crystallographic texture, which can be tied to flow stress via a crystal plasticity formalism that treats the sheet as an interacting aggregate of single crystal grains (Lebensohn and Tomé, 1993). A recent study found reasonable agreement between the measured and predicted yield surfaces using a variety of crystal plasticity based analyses (Hu et al., 2011) for multi-axial behavior of the as-received material deformed through monotonic linear strain paths. This work is extended in the present study to determine if these modeling methods can be used to capture evolving flow stresses measured in sheet that is deformed along two sequential linear strain paths: equal-biaxial followed by uniaxial tension.

\* Corresponding author.

E-mail address: [mark.iadicola@nist.gov](mailto:mark.iadicola@nist.gov) (M.A. Iadicola).

## 2. Material

The material used in this investigation was industrially processed AA5754-O annealed sheet, nominally 1 mm thick. Its chemical composition is reported in Table 1. The grain diameter in the rolling plane is approximately 40  $\mu\text{m}$ . The alloy derives its strength from the solid solution strengthening, with magnesium atoms interacting with dislocations and inhibiting dynamic recovery processes during straining. At room temperature, this alloy is known to exhibit yield point behavior and the Portevin-Le Chatelier (PLC) effect in its mechanical response (Kang et al., 2006). This effect is also seen in the data discussed in this work. The crystallographic texture of the as-received (AR) material is measured using an X-ray diffraction technique on a conventional diffractometer with quarter-circle Euler cradle, Cu  $K\alpha$  radiation, and a multiwire area detector. Fig. 1(a) is a plot of the  $\{111\}$  pole figure with the rolling direction (RD) on the horizontal axis and the direction transverse to the rolling direction (TD) on the vertical axis. Fig. 1(b) presents two significant sections of the orientation distribution function (ODF) expressed by Euler angles,  $\phi_1$ ,  $\Phi$ , and  $\phi_2$  (in Bunge's notation). These sections show the AR material initially has a weak texture, mainly the recrystallization Cube component  $\{100\}\langle 001\rangle$  and rolling texture components along the  $\beta$  fiber (Brass  $\{011\}\langle 211\rangle$  to  $S\{123\}\langle 634\rangle$  and to Copper  $\{112\}\langle 111\rangle$ ).

## 3. Experimental procedures and results

Samples were tested through linear and bi-linear strain paths, as shown in Fig. 2. As-received samples were strained in equal-biaxial and uniaxial tension to near failure. Other samples were strained in two segments: Segment 1, equal-biaxial tension to prescribed strain levels and then in Segment 2, strained in uniaxial tension in one of two orthogonal directions, the rolling direction (RD) or transverse to the rolling direction (TD).

A modified form of the Marciniak cup test is used to deform the as-received samples in equal-biaxial strain (tension) to near failure (Foecke et al., 2007). The tooling used includes an axisymmetric ram 200 mm in diameter with a 12 mm radius bead along its edge and a binder with lock bead. There is no direct method to calculate stress from the measured punch force, due to unquantifiable friction; therefore, a method of stress determination through X-ray diffraction (XRD) measurements, carried out during holds in the deformation, was performed on the surface of the sample above the centerline of the ram (Iadicola et al., 2008). This method requires calibration of the effective X-ray elastic constant (Noyan and Cohen, 1987; Iadicola and Gnäupel-Herold, 2012), which was accomplished using uniaxial testing as described below. Plastic strains for all of the biaxial samples were measured using a calibrated compact biaxial extensometer mounted slightly off the center of the specimen (Iadicola et al., 2008). Fig. 3 is a plot of the measured equal-biaxial true-stress true-strain data for four experiments, two experiments in each direction: RD and TD. The uncertainties shown for each data point are based on the larger of either the systematic error or the quality of the XRD measurement scan.

**Table 1**

Chemical composition of as-received AA5754-O determined using ASTM E227.

| Element                    | Mass fraction $\times 100$ |
|----------------------------|----------------------------|
| Mg                         | 3.75                       |
| Mn                         | 0.29                       |
| Fe                         | 0.24                       |
| Si                         | 0.06                       |
| Cr, Cu, Pb, Ni, Sn, Ti, Zn | Individually $<0.05$       |
| Aluminum                   | Balance                    |

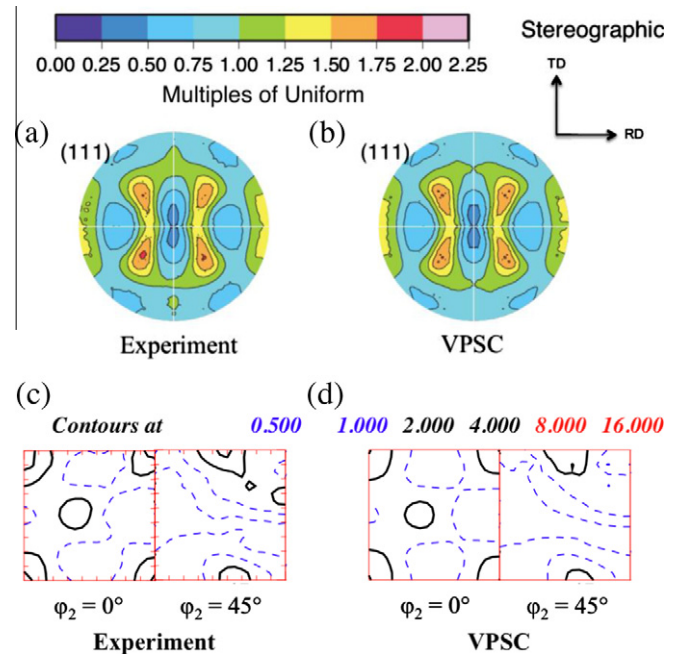


**Fig. 1.** Recalculated  $\{111\}$  pole figures for as-received AA5754-O (a) measured and (b) fitted input for VPSC model. The unit of intensity is multiples of a uniform distribution. Orientation distribution function sections for as-received AA5754-O (c) measured and (d) fitted input for VPSC model.

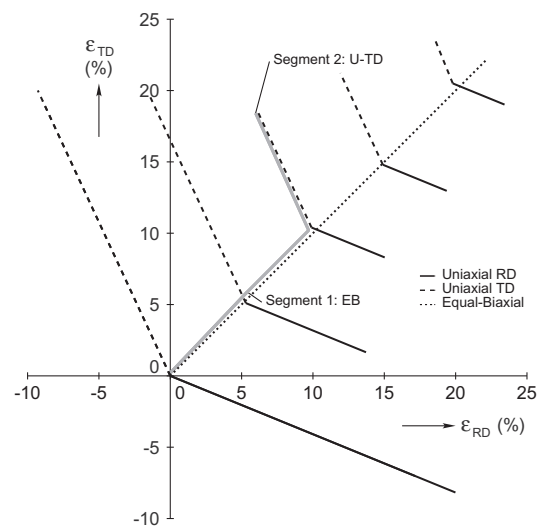


**Fig. 2.** Linear strain paths plotted along true-strain axes: equal-biaxial (dotted), uniaxial RD (solid), and uniaxial TD (dashed). Example of two segment forming shown in grey where Segment 1 is equal-biaxial straining to approximately 10% true-strain followed by Segment 2 uniaxial straining in the TD.

The repeat tests showed good agreement when considering the uncertainties of the measurements. The Marciniak method described above imposes near equal-biaxial strain to the specimen, but due to the orthotropic nature of rolled sheet metal, the stresses relating to these strains are found to be different for the two (RD and TD) directions.

Uniaxial specimens in the RD and TD were machined to the ASTM E-8 sub-size geometry for sheet metals. Some as-received (AR) samples were tested by standard methods using an 88 kN electro-mechanical testing machine with calibrated load cell, axial extensometer, and transverse extensometer. Three repeat tests in

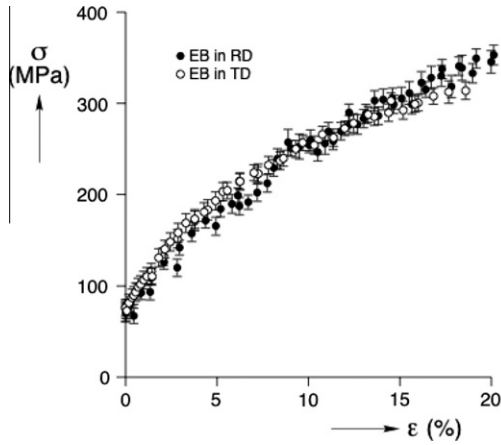


**Fig. 3.** Measured equal-biaxial true-stress true-strain data RD (solid circles) and TD (open circles), measured using XRD for two experiments in each direction (Iadicola et al., 2008).

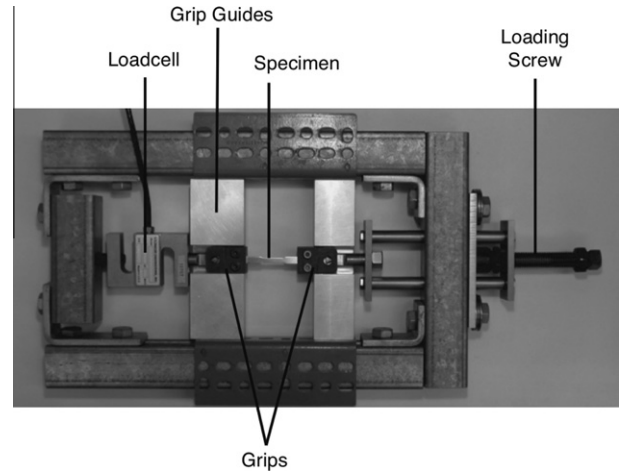


**Fig. 5.** Compact testing frame for uniaxial testing with simultaneous X-ray diffraction.

each orientation (RD and TD) showed excellent agreement (within ±4 MPa). The results of a single representative test, in each direction (RD and TD), are shown in Fig. 4 as solid lines. The yield point phenomena (in TD) and serrated yielding associated with the PLC effect (in RD and TD) are visible in the stress–strain curves. Four AR samples were tested using a compact testing frame (Fig. 5) and also with a calibrated load cell and axial extensometer, with the addition of the XRD stress determination. In Fig. 4, the results of two of these interrupted XRD samples (one RD and one TD, shown as circles) are compared with those of the continuously strained standard test results, (solid lines) and show excellent agreement, typically within the serrated flow stress variation. The effective X-ray elastic constants (XECs) used in these measurements were partially verified using similar tests with frequent elastic unload–reload cycles during plastic deformation, as shown in Fig. 6. The stresses during the elastic unloads were always above 80% of the initial yield stress, with the exception of two complete unloads at the end of a day of testing when the samples were stored at freezer temperatures (<−15 °C) overnight to reduce any room temperature recovery. The variation of effective XEC,  $1/2 S_2$ , from the average value was found to generally be within the uncertainty of the measurements in the range of testing, as shown in Fig. 7 (Iadicola and Gnäupel-Herold, 2012).

In the bi-linear strain path tests Segment 1, the Marciniak method and biaxial extensometer described above were used to strain as-received samples to target levels of 5%, 10%, 15%, and

20% true-strain in each direction (along the dotted path in Fig. 2), resulting in equivalent strains of approximately 10%, 20%, 30%, and 40% true-strain, respectively. The equivalent strains are calculated using the von Mises effective strain of  $\sqrt{\frac{2}{3} \epsilon_{ij} \epsilon_{ij}}$  where  $\epsilon$  is the plastic strain tensor, of which the non-zero components are generally those corresponding to the stretches in the RD, TD, and sheet normal direction (ND), and  $\epsilon_{ND}$  is calculated from the other strains assuming volume conservation. In the remainder of this paper, we will describe results in terms of the true-strain measured in the direction of interest, not in terms of the equivalent strain. After achieving the prescribed strains, the Marciniak samples were unloaded and trimmed as shown in Fig. 8 for use in multiple studies including crystallographic texture development (Banovic et al., 2008), surface roughening (Stoudt et al., 2009; Hubbard et al., 2011), XEC determination (Iadicola and Gnäupel-Herold, 2012), and the bi-linear strain path results shown here. The uniaxial samples for Segment 2 were mechanically machined from the Marciniak strained specimens in the RD and TD (Fig. 8) to a shape similar to the ASTM E-8 sub-size geometry (with shorter end tabs). No effort was made to prevent room temperature recovery of the samples after unloading from equal-biaxial straining. The samples were stored at room temperature for approximately 6 months before Segment 2 machining and testing.

In the Segment 2 tests, the biaxial strained and trimmed samples were tested using the compact uniaxial frame with the calibrated axial extensometer, calibrated load cell, and the XRD system for

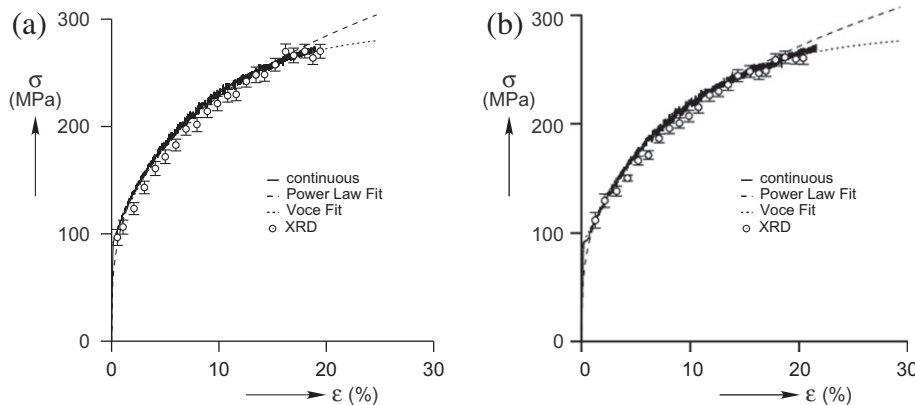


**Fig. 4.** AR uniaxial true-stress vs. true-strain plots for (a) RD and (b) TD. Solid lines are a representative test results for continuously strained samples and data points are data from XRD stress measurement during extension holds using compact testing frame and measured effective XEC (Iadicola et al., 2008).

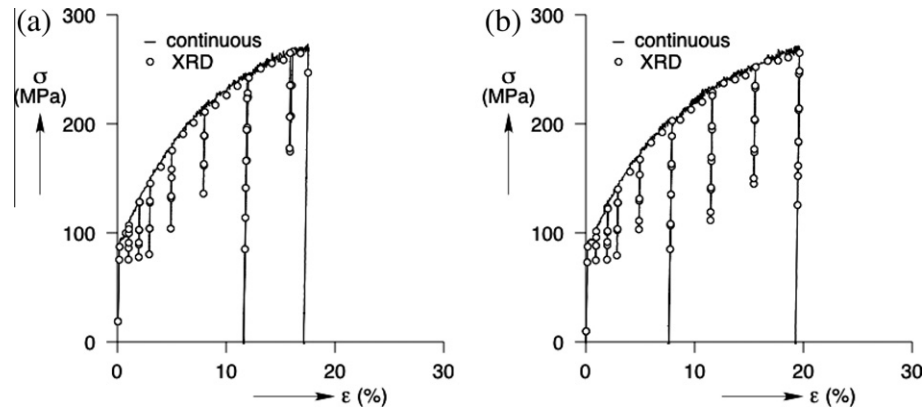


Fig. 6. Uniaxial true-stress vs. true-strain results with frequent holds for XRD measurement for (a) RD and (b) TD samples. Solid lines are data from load cell and extensometer and data points are data from XRD stress measurement using compact testing frame and calibrated effective XEC.

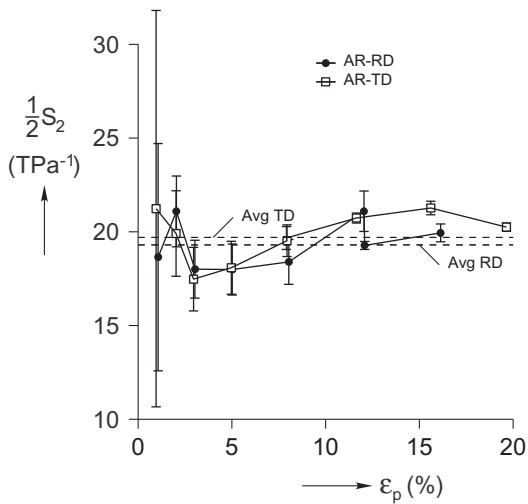


Fig. 7. Variation of effective XEC ( $\frac{1}{2} S_2$ ) with plastic strain for as-received samples in RD and TD.

stress determination similar to the AR uniaxial effective XEC tests described above. The testing cycle included plastic deformation followed by elastic unload-reloads (while stress levels were kept above 80% of the AR initial yield stress) followed by further plastic straining (similar to Fig. 6 for the AR material). This permitted

determination of effective XEC after the biaxial deformation. The results showed similar behavior to the variation of effective XEC in Fig. 7. Therefore a single average value was used in each direction (RD and TD, dashed lines in Fig. 7) (Iadicola and Gnäupel-Herold, 2012). From the load cell and axial extensometer measurements, during these same tests, the Segment 2 continuous mechanical responses were derived and are shown in Fig. 9(a) and (b) for RD and TD, respectively. In Fig. 9, the unload-reload portions have been removed and the initial elastic loading is shown dotted. Dashed red lines show the Voce fit to the AR uniaxial data (from Fig. 4) and the AR equal-biaxial data (from Fig. 3) for comparison of the AR monotonic material response to the bi-linear response. The Segment 2 maximum uniform strain (the maximum strain for the solid lines in Fig. 9) decreases with increased Segment 1 strain, but the entire response is more of interest in this paper. The crystal plasticity model results for the two segment process are compared to these data, through a combination of the AR equal-biaxial data up to the Segment 1 strain level and the plastic hardening portion of the uniaxial data (solid lines in Fig. 9) for straining during Segment 2.

4. Crystal plasticity constitutive analysis

The plasticity model used in this simulation is the Visco-Plastic Self-Consistent (VPSC) model developed by Tomé and Lebensohn at Los Alamos National Laboratory (Lebensohn and Tomé, 1993). The single-crystal constitutive behavior is given by

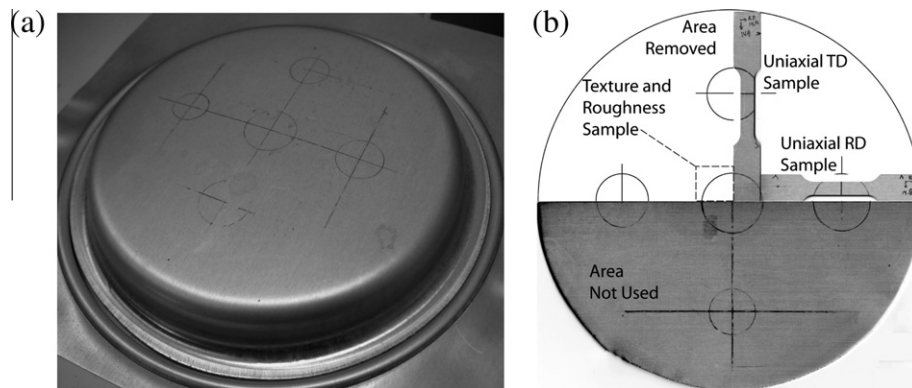
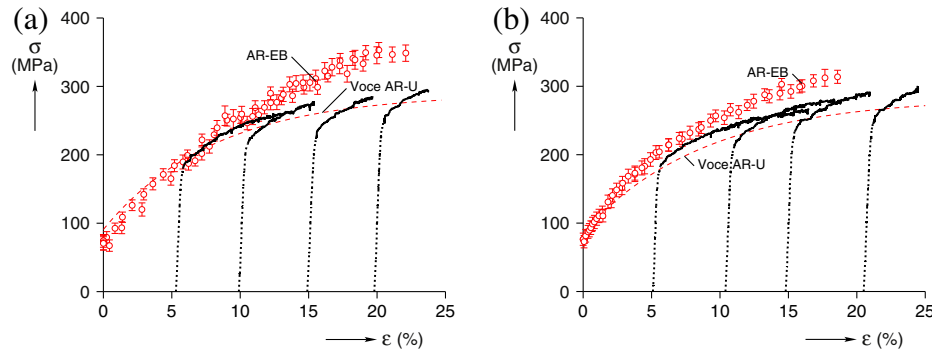


Fig. 8. Marciniak 200 mm diameter sample shape (a) after equal-biaxial 15% straining and (b) with areas trimmed for crystallographic texture measurement, surface roughness measurement, and subsequent uniaxial testing in RD and TD.



**Fig. 9.** Segment 2 uniaxial true-stress vs. true-strain plots after various levels of equal-biaxial straining in (a) RD and (b) TD, with initial elastic loading shown as dotted lines. For comparison, the Voce fit of the AR uniaxial data (from Fig. 4) and the AR equal-biaxial data (from Fig. 3) are shown in red as dashed lines and open circles, respectively. (For interpretation of the references to color in this figure legend, the reader is referred to the web version of this article.)

$$D_{ij}^g = \sum_{s=1}^N \dot{\gamma}_o \frac{m_{ij}^s}{(\tau_o^s)^n} (m_{kl}^s \sigma_{lk}^g)^\eta, \quad i, j, k = 1, 3 \quad (1)$$

$D^g$ , strain rate tensor;  $\sigma^g$ , stress tensor; the superscript  $g$  indicates that the tensors represent the state in each individual grain as opposed to the average stress in the material;  $N$ , number of slip systems;  $N$  is 12 for fcc crystals, allowing for both forward and backward slip; this is equivalent to 24 systems if separate entries are used for forward and backward slip;  $\dot{\gamma}_o$  reference shear rate;  $\tau_o^s$ , critical resolved shear stress (CRSS) of the slip system  $s$ ;  $\eta$  the inverse of the rate sensitivity exponent, which is set to 20 in this work;  $m^s$ , Schmid tensor of slip system  $s$  defined as  $m_{ij}^s = \frac{1}{2}(b_i n_j + b_j n_i)$ , where  $b$  is the slip direction and  $n$  is the slip plane normal.

The VPSC model deals with the interaction of grains by introducing a homogeneous effective medium (HEM). It treats each grain as a visco-plastic ellipsoidal inclusion embedded in and interacting with the effective medium. The stress and strain in the grains can vary as a function of orientation, depending on the stiffness of the interaction. The properties of the HEM are not known *a priori* and are adjusted self-consistently to coincide with the average of all inclusions forming the aggregate. As a result, the stress equilibrium and deformation compatibility conditions are satisfied in an average sense. The tangent linearization scheme is adopted in this simulation.

Metals generally strengthen with plastic deformation. Several mechanisms contribute to the increase in strength, and those considered in this work include primary work-hardening, latent hardening and kinematic hardening. In the latent hardening theory, non-active systems harden differently from the active systems. Kinematic hardening is the softening of a slip system upon strain reversal. Incorporating anisotropic hardening behaviors, the strain hardening behavior of the material can be described by the evolution of the CRSS on each slip system in the plasticity model according to the following,

$$\dot{\tau}_\alpha = \frac{d\tau_\alpha}{d\gamma} \sum_{\beta=1}^N q_{\alpha\beta} \dot{\gamma}_\beta \quad (2)$$

where  $d\gamma$  is the increment of shear on the slip system.  $\dot{\tau}_\alpha$  is the hardening rate on the slip system  $\alpha$ , which is related to the shear rate  $\dot{\gamma}_\beta$  on all the slip systems.  $q_{\alpha\beta}$  is an empirical hardening coefficient matrix that accounts for the interaction among the  $N$  slip systems. Eq. (2) is used in this work to incorporate latent hardening and kinematic hardening behaviors. This equation reduces to the isotropic hardening if the hardening coefficients equal one everywhere.

The increase of the CRSS from primary work-hardening is given by an extended Voce hardening law,

$$\tau = \tau_0 + (\tau_1 + \theta_1 \gamma) \left( 1 - \exp \left( -\gamma \left| \frac{\theta_0}{\tau_0} \right| \right) \right) \quad (3)$$

where  $\gamma$ ,  $\tau_0$ ,  $(\tau_0 + \tau_1)$ ,  $\theta_0$ , and  $\theta_1$  are the accumulated slip (shear), the initial CRSS, the back-extrapolated CRSS, the initial hardening rate, and the asymptotic hardening rate on each slip system, respectively. The additional residual hardening rate of  $\theta_1$  has a small value that allows for Stage IV hardening to be modeled, which is the small but finite and constant hardening observed out to very large strains in almost all metals at low homologous temperatures.

The initial texture (Fig. 1) was incorporated into the plasticity simulation using a set of 24,938 weighted orientations derived from the measured texture (Kallend et al., 1991). The experimental stress–strain curves used to identify the strain hardening parameters include AR RD uniaxial tension, AR TD uniaxial tension, AR equal-biaxial in the RD and TD, and the eight Segment 2 uniaxial tension curves (solid lines in Fig. 9) with varying levels of Segment 1 straining (four in each orientation). A single set of strain hardening parameters was identified to be the best match to all of these stress–strain curves simultaneously, which follows the principle that the mechanical behavior can be described at the single slip system level.

## 5. Model results and discussion

Previous plasticity simulation work was carried out to predict the stress–strain curves and texture evolution for five different monotonic strain paths, including uniaxial tension in the RD and TD, plane-strain in the RD and TD, and equal-biaxial stretch (Hu et al., 2011). In this work, a Voce-type isotropic hardening behavior similar to Eq. (3) was imposed in the VPSC simulation, and an optimal set of strain hardening parameters was determined to be a best fit to the experimental data. An underestimate of the flow stress for the equal-biaxial stretch test at higher strains was observed in that study. In order to improve the model prediction, a Stage IV hardening behavior has been incorporated into the

**Table 2**

Strain hardening parameters for VPSC model fitted to AR multi-axial behavior (top row), or all the available AR uniaxial, AR equal-biaxial, and bi-linear strain path data (bottom row).

| Hardening | $\tau_0$ (MPa) | $\tau_1$ (MPa) | $\theta_0$ (MPa) | $\theta_1$ (MPa) | $q_{\text{latent}}$ | $q_{\text{kinematic}}$ |
|-----------|----------------|----------------|------------------|------------------|---------------------|------------------------|
| Isotropic | 36             | 63             | 307              | 30               | 1                   | 1                      |
| Latent    | 41             | 81             | 318              | 21               | 0.6                 | 1                      |

simulation, as described by  $\theta_1$  in Eq. (3) and fitted to AR multi-axial behaviors. Using the material parameters identified (top row in Table 2), an initial trial of the stress–strain curve calculation for the

strain-path change tests on the same sheet aluminum alloy was performed using the isotropic hardening only. Fig. 10 shows the comparison between the VPSC predictions and the experimental

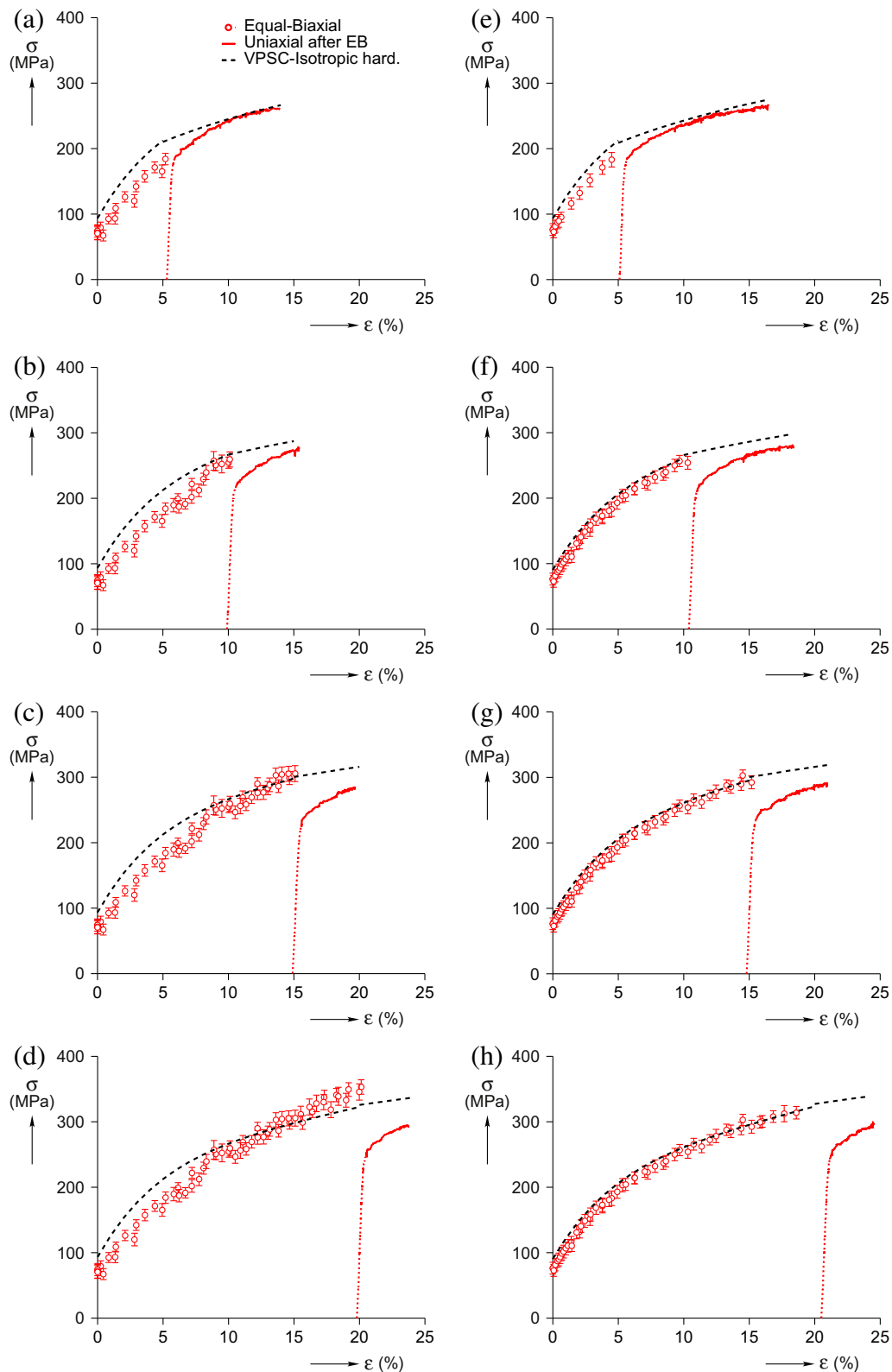


**Fig. 10.** Comparison of the experimental stress–strain data (AR equal-biaxial, red circles, and Segment 2 uniaxial, red line) and the VPSC predictions (dashed black lines) with isotropic hardening only. Plots are combined results for Segment 1 equal-biaxial and Segment 2 uniaxial tension in RD after (a) 5%, (b) 10%, (c) 15%, and (d) 20% Segment 1 straining, and in TD after (e) 5%, (f) 10%, (g) 15%, and (h) 20% Segment 1 straining. (For interpretation of the references to color in this figure legend, the reader is referred to the web version of this article.)

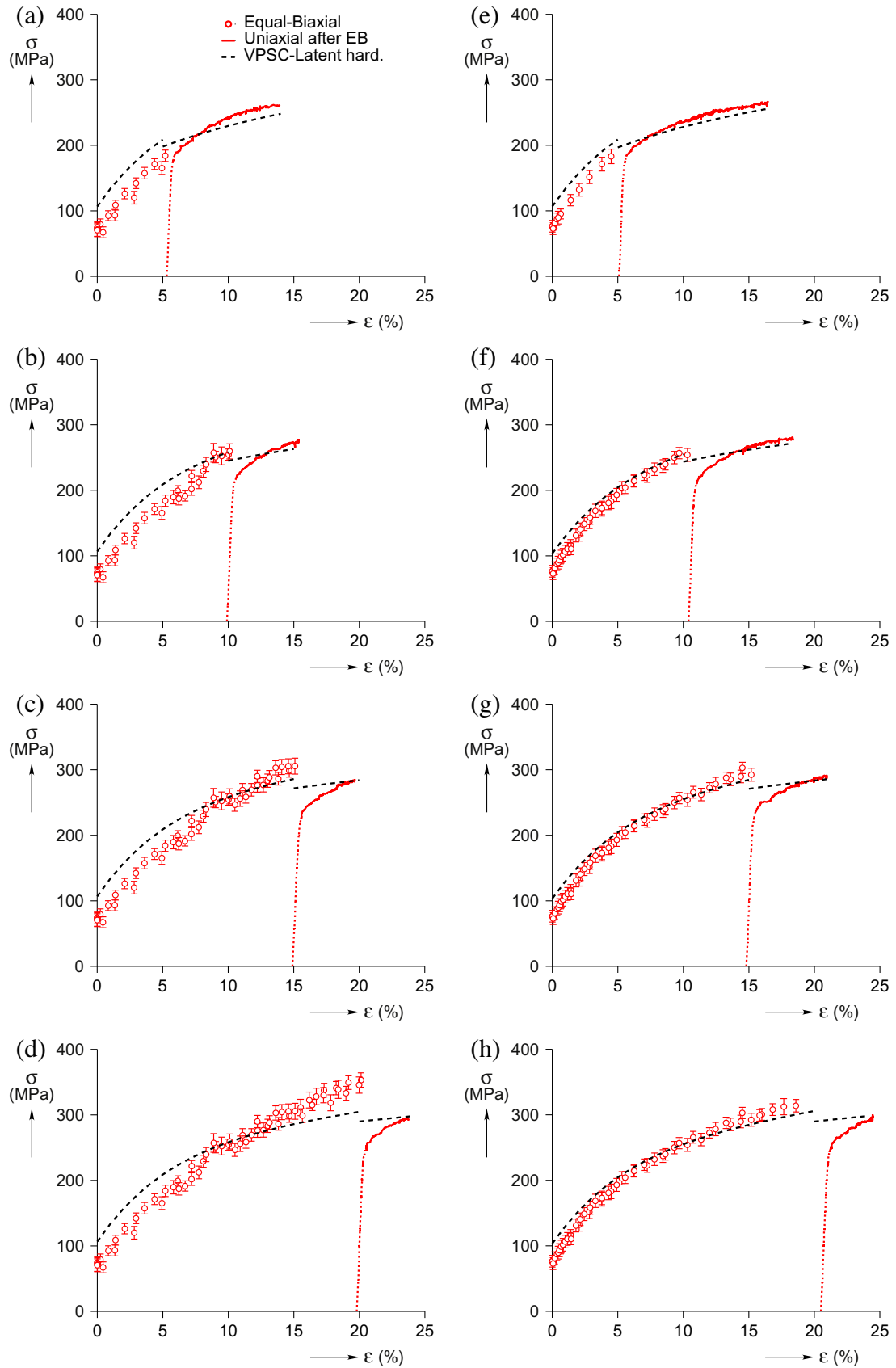


**Fig. 11.** Comparison of the experimental stress–strain data (AR equal-biaxial, red circles, and Segment 2 uniaxial, red lines) and the VPS predictions (dashed black lines) incorporating latent hardening. Plots are combined results for Segment 1 equal-biaxial and Segment 2 uniaxial tension in RD after (a) 5%, (b) 10%, (c) 15%, and (d) 20% Segment 1 straining, and in TD after (e) 5%, (f) 10%, (g) 15%, and (h) 20% Segment 1 straining. (For interpretation of the references to color in this figure legend, the reader is referred to the web version of this article.)

**Table 3**

Room temperature approximately (21 °C) recovery data for uniaxial straining in RD after equal-biaxial (EB) strain to approximately 5% true-strain. Yield stress at 0.002 strain-offset ( $\sigma_y$ ), ultimate tensile strength (UTS = maximum engineering stress), and engineering strain at UTS ( $e_{UTS}$ ) are reported for the uniaxial Segment 2 with varying time at room temperature. Specimen time not at room temperature for all samples was at freezer temperatures (<−15 °C).

| Time at room temp.   | 20 min    | 2 weeks   | 6 months  |
|----------------------|-----------|-----------|-----------|
| EB true-strain (m/m) | 0.054     | 0.055     | 0.053     |
| $\sigma_y$ (MPa)     | 232 ± 3   | 213 ± 3   | 171 ± 3   |
| UTS (MPa)            | 247 ± 4   | 249 ± 4   | 239 ± 2   |
| $e_{UTS}$ (%)        | 5.4 ± 1.2 | 5.8 ± 0.7 | 8.1 ± 0.7 |

curves. The model predicted a slight increase of the flow stress upon the strain path change from Segment 1 to Segment 2, whereas the experiment shows a much larger decrease. The model also was not able to capture the high hardening rate at the initial portion of Segment 2 plastic deformation seen in the experimental curves.

Strain path changes often involve activations of formerly latent slip systems, and possibly slip system reversals. The large discrepancy between the isotropic hardening model prediction and the experimental data demonstrate that anisotropic hardening behaviors must be added to the analysis.

Plastic deformation occurs on the  $\{111\}$ – $\langle 110 \rangle$  slip systems in FCC materials. Considering both forward and backward slip (i.e., two slip systems on the same slip plane but along opposite slip directions), there are 24 slip systems. Since the latent hardening is considered to be induced by the interaction between the mobile dislocation and the forest dislocations, the slip systems are divided into four coplanar groups associated with four  $\{111\}$  planes:  $(111)$ ,  $(1-11)$ ,  $(11-1)$ ,  $(-111)$ . The different types of interactions between the slip systems are categorized into three groups:  $q_{\alpha\beta} = q_{self} = 1$ , if  $\alpha$  and  $\beta$  are coplanar but not a forward and backward slipping pair;  $q_{\alpha\beta} = q_{latent} \neq 1$ , if  $\alpha$  and  $\beta$  are non-coplanar;  $q_{\alpha\beta} = q_{kinematic} < 1$ , if  $\alpha$  and  $\beta$  are a forward and backward slipping pair. The fitted material parameters are shown in the bottom row of Table 2.

The slip system activities were investigated to determine whether kinematic hardening behavior is relevant in this simulation. The model simulated a uniaxial tension in the RD after a 15% equal-biaxial Segment 1 straining. The calculated shear strains on

slip systems that reverse during the strain path change were recorded and normalized by the total strain in the grain. An average of only 0.31% of such normalized shear strains was found. Varying the Segment 1 strain levels was also analyzed, but the effect was found to be negligible. We concluded that kinematic hardening does not play a role in this particular type of strain path change, and the kinematic hardening coefficient  $q_{kinematic}$  is therefore set to 1.

Latent hardening is included in the plasticity modeling to capture possible anisotropic hardening behaviors. A statistical best fit was found when  $q_{latent} = 0.6$ . The calculated stress–strain curves are shown in Fig. 11. By incorporating the latent hardening, the model successfully predicted a flow stress decrease upon the strain path change. However, even with taking latent hardening into account, the simulation still does not fully capture the transient softening upon the strain path change.

Literature studies (Go, 2001; Halim et al., 2007) have reported that deformed Al–Mg alloys, similar to AA5754, recover measurably at room temperature for hold times longer than a day. Magnesium atoms pin dislocations, due to their high diffusivity during deformation, which severely retards dynamic recovery. This leads to a high stored energy, providing a large driving force for static recovery. It is possible that static recovery occurred in the Segment 1 strained samples during the six month time interval before they were tested in Segment 2, which along with anisotropic hardening behaviors, would also contribute to the increase in the hardening rate and decrease in the initial yield strength in the second loading. Three Segment 2 tests were performed with different amounts of time at room temperature (approximately 21 °C), to confirm the existence of recovery in the data being explored in this paper. Table 3 is a summary of these three tests that show the change in initial yield stress ( $\sigma_y$ ), ultimate tensile stress (UTS), and the engineering strain at the UTS ( $e_{UTS}$ ) with time at room temperature after equal-biaxial straining to about the same 5% true-strain. Both the decrease in initial yield stress and the increased hardening rate discussed above are seen with increased time at room temperature. Note: one can get an estimate of the average hardening rate based on  $(UTS - \sigma_y)/(e_{UTS} \times 100)$  resulting in 2.8 MPa, 6.2 MPa, and 8.4 MPa for recovery times of 2 min, 2 weeks, and 6 months, respectively. Taking account of this recovery effect may explain the transient behaviors observed during the strain path change. To fully understand the effects a complete experimental matrix and additional modeling is required, and is left for future work. It

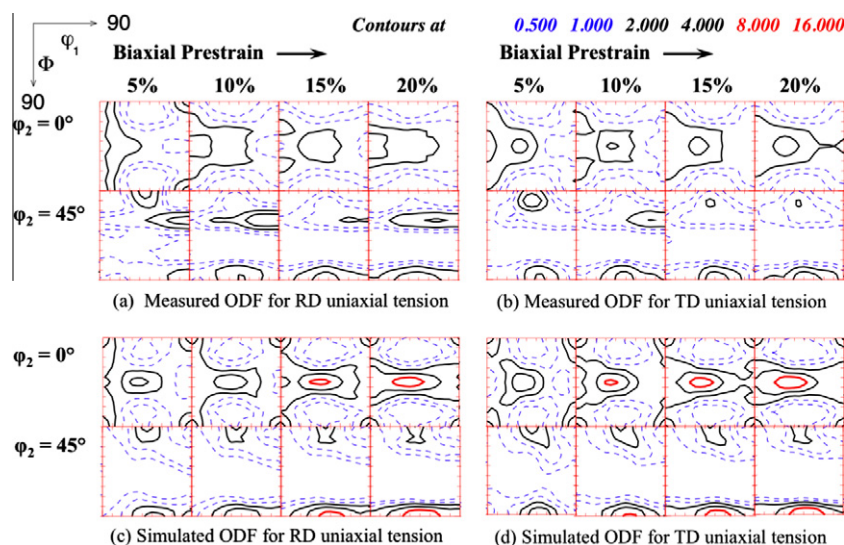


**Fig. 12.** Sections of ODF measured in RD and TD, (a) and (b) respectively, and simulated final texture in RD and TD, (c) and (d) respectively, in AA5754 samples after two segment process for four equal biaxial prestrain levels. 0 (top) and 45° (bottom)  $\phi_2$  ODF sections of the final texture are presented.

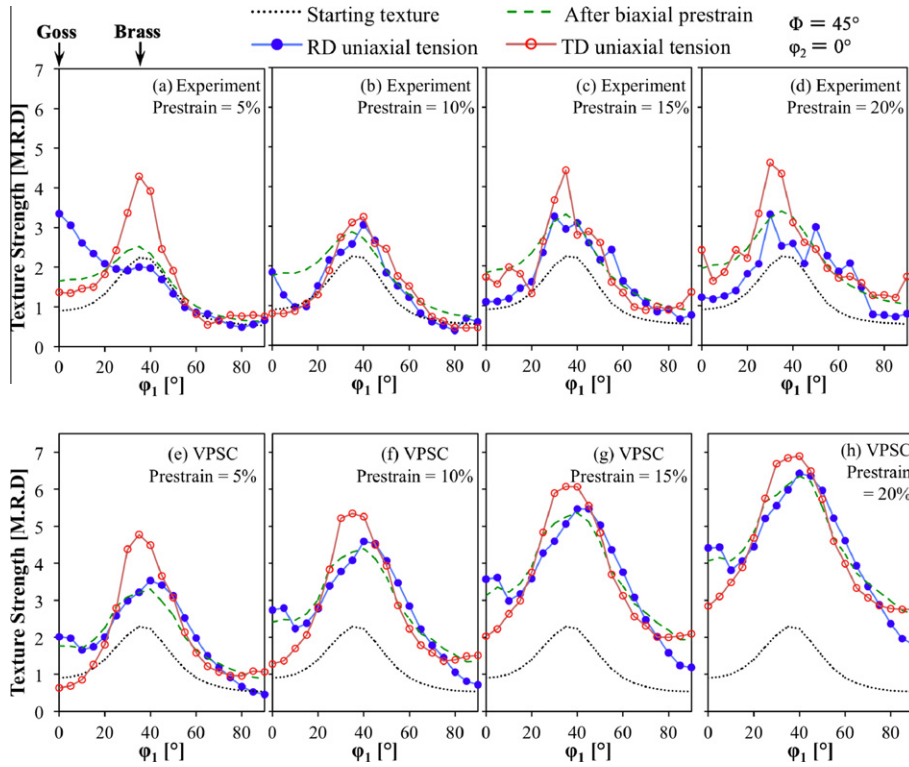


**Fig. 13.** Shows how volume fractions along the  $\alpha$  fiber ( $\phi_1 = 0\text{--}90^\circ$ ,  $\phi = 45^\circ$ ,  $\phi_2 = 0$ ) evolve during the two segments of deformation: the starting texture (black dotted line), the texture after biaxial straining (green dashed line), and the final texture after RD uniaxial tension (blue, solid circles), or TD uniaxial tension (red, open circles). Measured texture, (a)–(d), are compared to VPSC predictions, (e)–(h). All volume fractions are normalized by the values under a uniform texture, i.e., units of Multiples of a Random Density (M.R.D.). (For interpretation of the references to color in this figure legend, the reader is referred to the web version of this article.)

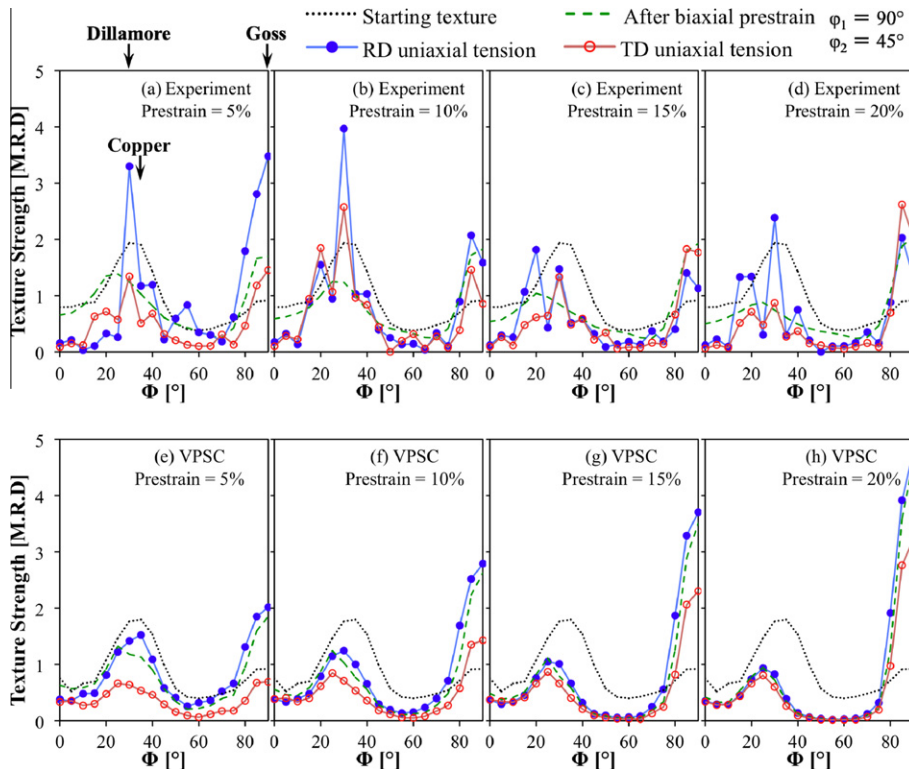


**Fig. 14.** Shows how volume fractions along the  $\tau$  fiber ( $\phi_1 = 90^\circ$ ,  $\phi = 0\text{--}90^\circ$ ,  $\phi_2 = 45^\circ$ ) evolve during the two segments of deformation: the starting texture (black dotted line), the texture after biaxial straining (green dashed line), and the final texture after RD uniaxial tension (blue, solid circles), or TD uniaxial tension (red, open circles). Measured texture, (a)–(d), are compared to VPSC predictions, (e)–(h). All volume fractions are normalized by the values under a uniform texture, i.e., units of Multiples of a Random Density (M.R.D.). (For interpretation of the references to color in this figure legend, the reader is referred to the web version of this article.)

is also significant that measurements of latent hardening (Franciosi et al., 1980; Wu et al., 1991) have reported parameter values greater than one, as might be expected for the hardening of non-active slip systems by the active ones. It seems likely, therefore, that the value of 0.6 reported here is affected by recovery.

The VPSC model gives a qualitatively correct texture prediction, but with higher texture intensities, which has been seen in previous studies (Hu et al., 2011). Fig. 12 shows ODF sections of measured and simulation final texture after deformation. After uniaxial tension, major texture components include the  $\alpha$  fiber (from equibiaxial stretch), Dillamore  $\{4\ 4\ 11\} \langle 11\ 11\ 8 \rangle$  and Copper (from uniaxial tension). Volume fractions along the  $\alpha$  fiber (Fig. 13) and the  $\tau$  fiber (Fig. 14) are calculated to quantify texture evolution. Equibiaxial stretch deformation produces a strong  $\alpha$  fiber texture that peaks at the Brass component, as seen in both the experimental and model results in Fig. 13. In the RD uniaxial tension following the equibiaxial stretch, grains gradually rotate towards the  $\langle 100 \rangle$  and  $\langle 111 \rangle$  fibers, leading to texture concentrations on components such as the Dillamore, Copper, and Goss components (as shown in Figs. 13 and 14). This change of  $\alpha$  fiber texture intensity profile is seen in both the experiment and the VPSC simulation. The change of the  $\tau$  fiber texture intensity profile for Copper and Dillamore components is stronger in the experimental textures than in the simulation. Note that the experimentally measured texture along this fiber shows some large variations near these components, which is not unexpected due in part to the uncertainties associated in measuring texture intensities. The final texture after TD uniaxial tension is primarily characterized by the strengthening of the Brass component, while grains rotate away from other components along the  $\alpha$  fiber (Fig. 13). This is well captured in the VPSC simulation.

## 6. Conclusions

The stress–strain response was measured in samples of aluminum alloy 5754 sheet subjected to various bi-linear strain paths, consisting of equal-biaxial tension followed by uniaxial tension. Simulations of the strain path change effect were performed using the Visco-Plastic Self-Consistent (VPSC) crystal plasticity model. It was found that incorporating latent hardening behavior improved the predictions of the mechanical response over simple isotropic hardening. Addition of kinematic hardening was found to not significantly change the results. The large hardening rate seen in the uniaxial response after equal-biaxial straining, at least partially a result of dynamic recovery, could not be effectively simulated using any of the hardening models. Experimental and predicted crystal texture development was qualitatively similar after the bi-linear strain path deformation, but did show some quantitative differences.

## Acknowledgements

The authors gratefully acknowledge ALCAN for the donation of the materials used in this study and the Intel Corporation for computing facilities.

## References

- Andar, M.O., Kuwabara, T., Yonemura, S., Uenishi, A., 2010. Elastic-plastic and inelastic characteristics of high strength steel sheets under biaxial loading and unloading. *ISIJ Int.* 50 (4), 613–619.
- Banovic, S.W., Iadicola, M.A., Foecke, T., 2008. Texture development of AA 5754 sheet deformed under in-plane biaxial tension. *Metall. Mater. Trans. A* 39A, 2246–2258.
- Choi, K.S., Liu, W.N., Sun, X., Khaleel, M.A., 2009. Microstructure-based constitutive modeling of TRIP steel: prediction of ductility and failure modes under different loading conditions. *Acta Mater.* 57, 2592–2604.
- Foecke, T., Iadicola, M.A., Lin, A., Banovic, S.W., 2007. A method for direct measurement of multiaxial stress–strain curves in sheet metal. *Metall. Mater. Trans. A* 38, 306–313.
- Franciosi, P., Berveiller, M., Zaoui, A., 1980. Latent hardening in copper and aluminum single-crystals. *Acta Metall.* 28, 273–283.
- Go, J., 2001. Recovery and recrystallization behavior of AA5754 and IF-Boron steel during annealing. PhD thesis. University of British Columbia.
- Halim, H., Wilkinson, D.S., Niewczas, M., 2007. The Portevin-Le Chatelier (PLC) effect and shear band formation in an AA5754 alloy. *Acta Mater.* 55, 4151–4160.
- Hosford, W.F., Duncan, J.L., 1999. Sheet metal forming: a review. *JOM-J. Minerals, Metals Mater. Soc.* 51 (11), 39–44.
- Hu, L., Rollett, A.D., Iadicola, M., Foecke, T., Banovic, S., 2011. Constitutive relations for AA 5754 based on crystal plasticity. *Metall. Mater. Trans. A* 43A (3), 854–869. <http://dx.doi.org/10.1007/s11661-011-0927-1>.
- Hubbard, J.B., Stoudt, M.R., Possolo, A., 2011. Topographic analysis and Weibull regression for prediction of strain localisation in automotive aluminium alloy. *Mater. Sci. Technol.* 27 (7), 1206–1212.
- Iadicola, M.A., Foecke, T., Banovic, S.W., 2008. Experimental observations of evolving yield Loci in biaxially strained AA5754-O. *Int. J. Plast.* 24 (11), 2084–2101.
- Iadicola, M.A., Gnäupel-Herold, T.H., 2012. Effective X-ray elastic constant measurement for in situ stress measurement of biaxially strained AA5754-O. *Mater. Sci. Eng.: A* <http://dx.doi.org/10.1016/j.msea.2012.02.100>.
- Kallend, J.S., Kocks, U.F., Rollett, A.D., Wenk, H.-R., 1991. Operational texture analysis. *Mater. Sci. Eng.* A132, 1–11.
- Kang, J., Wilkinson, D.S., Jain, M., Embury, J.D., Beaudoin, A.J., Kim, S., Mishra, R., Sachdev, A.V., 2006. On the sequence of inhomogeneous deformation processes occurring during tensile deformation of strip cast AA5754. *Acta Mater.* 54, 209–218.
- Kuwabara, T., 2007. Advances in experiments on metal sheets and tubes in support of constitutive modeling and forming simulations. *Int. J. Plast.* 23 (3), 385–419.
- Lebensohn, R.A., Tomé, C.N., 1993. A self-consistent anisotropic approach for the simulation of plastic-deformation and texture development of polycrystals – application to zirconium alloys. *Acta Metall.* 41 (9), 2611–2624.
- Noyan, I.C., Cohen, J.B., 1987. *Residual Stress*. Springer-Verlag, New York, pp. 57–74.
- Stoudt, M.R., Hubbard, J.B., Iadicola, M.A., Banovic, S.W., 2009. A study of the fundamental relationships between deformation-induced surface roughness and strain localization in AA5754. *Metall. Mater. Trans. A* 40A, 1611–1622.
- Stoughton, T.D., Zhu, X., 2004. Review of theoretical models of the strain-based FLD and their relevance to the stress-based FLD. *Int. J. Plast.* 20, 1463–1486.
- Yoshida, K., Kuwabara, T., Kuroda, M., 2007. Path-dependence of the forming limit stresses in a sheet metal. *Int. J. Plast.* 23 (3), 361–384.
- Wu, T.Y., Bassani, J.L., Laird, C., 1991. Latent hardening in single-crystals. 1. Theory and Experiments. In: *Proceedings of the Royal Society of London Series A-Mathematical Physical and Engineering Sciences*, vol. 435, pp. 1–19.